# Switching Acoustic Propagation via Underwater Metasurface

Peizheng Cao,[1] Yu Zhang,[1,2,3,*] Sai Zhang,[4] Wenzhan Ou,[1] Shahrzad Ghaffari Mosanenzadeh,[2] and Nicholas X. Fang[2]

[1] *Key Laboratory of Underwater Acoustic Communication and Marine Information Technology of the Ministry of Education, College of Ocean and Earth Sciences, Xiamen University, Xiamen, 361005, China*

[2] *Department of Mechanical Engineering, Massachusetts Institute of Technology, Cambridge, Massachusetts 02139, USA*

[3] *State Key Laboratory of Marine Environmental Science, Xiamen University, Xiamen 361005, China*

[4] *Department of Physics, Jiangsu University, Zhenjiang 212013, China*

(Received 7 November 2019; revised manuscript received 14 January 2020; accepted 5 March 2020; published 8 April 2020)

Switching on and off acoustic waves through metamaterials has potential in noise canceling, underwater detection, and communication. However, traditional acoustic designs are challenging in manipulating underwater acoustic waves when the device thickness is less than wavelength. Here we report an alternative design of an underwater metasurface-based acoustic switcher to achieve this goal. The switching mechanism is revealed by combing acoustic diffraction of grating with mode conversion of double-layer PMMA plates. The device is tuned to control wave transmission by changing grating angle. Furthermore, we experimentally fabricate the metasurface acoustic switcher. The broadband-switching performance is realized to control underwater target detection and to produce binary digital encoding for acoustic waves. The proposed metasurface acoustic switcher offers the advantages of broadband performance and thin structure, which promises the opportunity for designing next-generation broadband-switching devices in underwater acoustic detection and communication.

DOI: 10.1103/PhysRevApplied.13.044019

## I. INTRODUCTION

In comparison with the high attenuation of optical and electromagnetic waves in sea waters, acoustic wave readily propagates for thousands of kilometers. The demand for new materials to manipulate acoustic waves is increasing in underwater communication, navigation, and imaging applications. Acoustic metamaterials with specific material function designs can produce fascinating phenomena [1–7], and their promising applications are acoustic cloaking in target detection [8,9], acoustic diode in asymmetric sound transmission [10], and spiral acoustic multiplexing technology in communication [11]. Metasurfaces regarded as the lower-dimensional correspondence of metamaterials, may provide a promising solution [12,13]. Metasurface thin structure is composed of microstructures arranged in a specific spatial distribution to produce designed reflection or transmission [14,15]. In underwater conditions, metasurfaces have a significant advantage of thin layers, and provide a promising path for applications in thin-structure beam steering, tunable lenses, and acoustic cloaking.

Motivated by the on-off mechanism of electric switches, acoustic switching has recently been proposed to turn on and off the band gaps by Bragg scattering or local resonance [2]. Babaee *et al*. applied a deformable periodic material of elastomeric helices to switch on and off the propagation of sound [16]. The investigation of underwater acoustic switching has potential applications in noise canceling, sonar detection control, and digitizing acoustic waves for communication.

In this paper, we report another class of underwater metasurface acoustic switcher (MAS) to control *on* and *off* in wave propagation. The structure is composed of an acoustic grating and double-layer PMMA plates, which can be regarded as an underwater metasurface. Acoustic mode conversions of the PMMA-water structure are theoretically derived. Acoustic diffraction of grating and forbidden transmission of MAS contribute to the switching mechanism, as verified by full-wave simulations. MAS is tuned to control wave transmission by changing the grating angle. Furthermore, we experimentally fabricate MAS and achieve broadband switching. The device is then applied to control underwater acoustic target detection and to produce binary digital encoding.

## II. RESULTS AND DISCUSSION

We design the MAS structure by integrating a vertical acoustic grating and a horizontal double-layer PMMA plates in water background [Fig. 1(a)]. The grating is an

*yuzhang@xmu.edu.cn

 

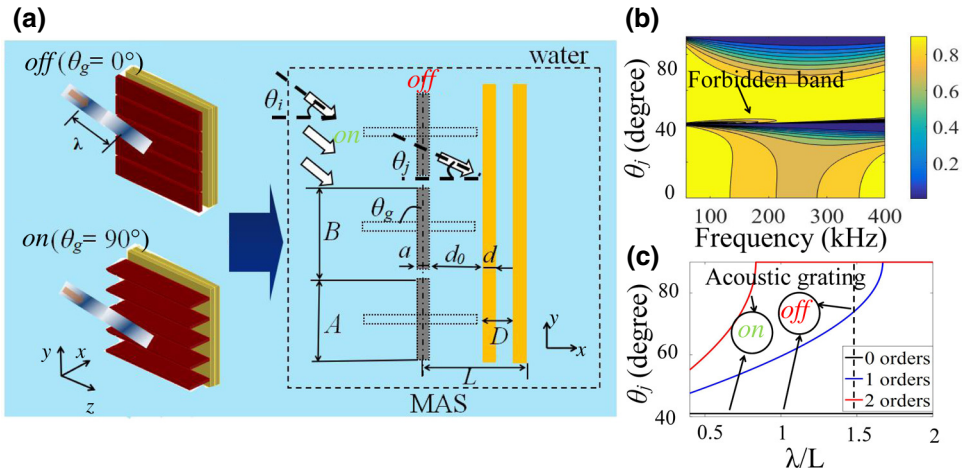


FIG. 1. Underwater metasurface acoustic switcher. (a) Systematic diagram of the MAS structure. (b) Transmission coefficient with respect to frequency and incident angle, where $N = 2$. (c) Relationship between diffraction angle and normalized wavelength $\lambda/L$.

array of steel blocks with length $A$, thickness $a$, and grating angle $\theta_g$. The distance $B$ between two steel blocks gives the grating filling rate as $A/B$. Each PMMA plate has the thickness $d$ and the distance between double plates is $D$. The distance between acoustic grating and PMMA is the coupling distance $d_0$. According to the experiments, we set the following structural and material parameters in the design as follows: $a = 3$ (mm), $A = 15$ (mm), $d_0 = 5.5$ (mm), $d = 3$ (mm), $B = 16$ (mm), $D = 4$ (mm), Young's modulus $E_s = 2.16 \times 10^{11}$ (N/m$^2$), Poisson's ratio $\delta_s = 0.28$, density $\rho_s = 7800$ (kg/m$^3$) for steel, $E_{\mathrm{PMMA}} = 5.35 \times 10^{10}$ (N/m$^2$), $\delta_{\mathrm{PMMA}} = 0.35$, $\rho_{\mathrm{II}} = 1180$ (kg/m$^3$) for PMMA, $\rho_{\mathrm{I}} = 998$ (kg/m$^3$), sound speed $c_w = 1482$ (m/s) in water. The overall thickness of MAS is $L = 12.5$ (mm), which is smaller than the wavelength $\lambda$ in water for the frequency range applied in this study. Thus, MAS is considered as metasurface. We define *on* by MAS with grating angle $\theta_g = 90°$ and *off* by MAS with $\theta_g = 0°$.

For *off* configuration, $A \approx B$ leads to the almost closed acoustic grating. The steel grating can be regarded as the sound barrier of MAS. A plane wave with incident angle $\theta_i$ passes though the grating and propagates within the PMMA. As shown in Fig. 1, $\theta_i \approx 41°$ is used for MAS. Acoustic mode conversion then appears. To show this, we apply the transfer matrix method of the PMMA, as shown in Fig. 6 in the Appendix, where $x$ and $y$ axes are normal and parallel to the interfaces, respectively, and a plane longitudinal wave propagates from the left side and travels to the right side. In water medium, compressional waves satisfy the wave equation $(1/\rho_{\mathrm{I}} c_w^2)(\partial^2 p)/\partial t^2) + \nabla \cdot [-(1/\rho)\nabla p] = 0$, where $p$ is the sound pressure. While PMMA plates lead to the shear waves satisfying $\rho_{\mathrm{II}}(\partial^2 \mathbf{v}/\partial t^2) = (\lambda' + \mu')\nabla(\nabla \cdot \mathbf{v}) + \mu' \nabla^2 \mathbf{v}$, where $\mathbf{v}$ is the velocity vector, $\lambda'$ and $\mu'$ are two Lamé constants. Longitude wave in water passes through the liquid-solid interface, and then is converted to longitude and shear waves in PMMA [17,18]. These waves are further converted back to the longitudinal wave through the liquid-solid interface. The transmission coefficients with respect to incident angle and frequency are given for comparison with $N = 1$, 2, 5, and 10, as shown in Figs. 1(b) and 7 in the Appendix. The boundary conditions of the plates lead to Lamb waves with various modes, such as symmetric and asymmetric types. Symmetric modes are characterized by longitudinal vibration of the center particle of the thin plate, while the asymmetric modes are characterized by transverse vibration [19]. In particular, within a specified angle range of $\theta_i \approx 41°$, forbidden band transmissions due to multiple scattering of low-order Lamb wave modes [7] of thin plates in water are found at low frequencies. Such forbidden bands can also be observed at higher frequencies due to Brag scattering. Thus, MAS achieves the function of closing. This phenomenon cannot be observed in the PMMA-air metamaterial [Fig. 6(b)], suggesting the unique property of MAS.

However, for *on* configuration, the acoustic grating is opened. It diffracts the incident wave to various propagation directions. The $j$-order diffraction mode with the diffraction angle $\theta_j$ satisfies the grating equation as follows: $B(\sin\theta_j - \sin\theta_i) = j\lambda$ $(j = 0, 1, 2\ldots)$ [20]. $\theta_j$ increases with $\lambda$ and $j$, but approaches 90° for sufficiently large $\lambda$ [Fig. 1(c)]. $\theta_j$ is larger than $\theta_i$, suggesting that the wave front of the incident wave is distorted. When $\theta_j$ deviates from the forbidden band of the PMMA-water system, high-order diffraction waves enter the pass band so that high transmission appears. MAS then achieves the function of opening.

We further perform full-wave simulations to examine acoustic switching of MAS by using COMSOL Multiphysics. A plane wave with an incident angle of $\theta_i = 41°$ and frequency of 80 (kHz) (corresponding to $\lambda/L = 1.5$) incidents from the left side of the structure. For *off* configuration ($\theta_g = 0°$), the forbidden transmission leads to negligible intensity in the right side [Fig. 2(a)]. However, for *on* configuration ($\theta_g = 90°$), a wave pattern appears on the right side.

MAS can be tuned by changing the grating angle $\theta_g$ as well as the angle $\theta_i$, as shown in Fig. 2(b). The

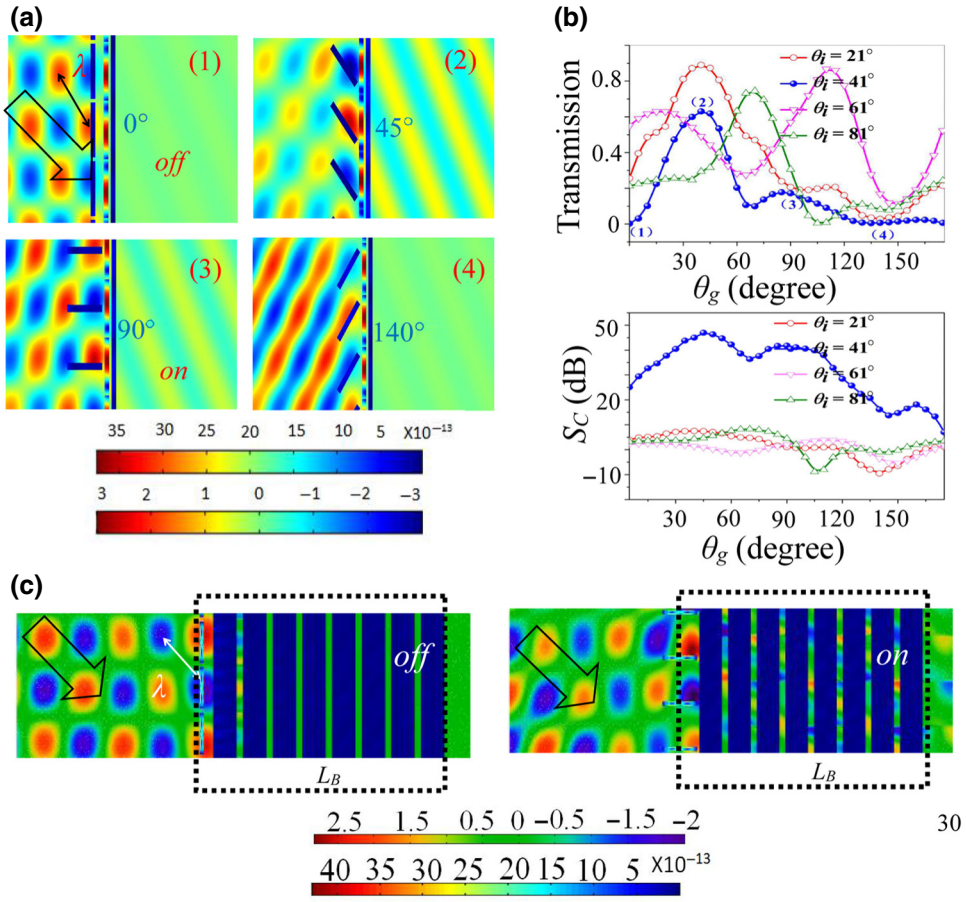


FIG. 2. (a) Acoustic pressure and displacement distributions of MAS at grating angles 0° (*off*), 45°, 90° (*on*), and 140°, where $f = 80$ (kHz) and $\theta_i = 41°$. (b) Dependencies of grating angle $\theta_g$ on transmission coefficient and the coefficient of switch of MAS for $\theta_i = 21°$, 41°, 61°, 81°, respectively, where (1), (2), (3), and (4) corresponds to the grating angles in (a). (c) Acoustic pressure and displacement distributions by switching *off* and *on* the Bragg scattering system, where eight layers ($N = 8$) are used.

corresponding acoustic fields at $\theta_g = 0°$ (*off*), 45°, 90° (*on*) and 140° are given in Fig. 2(a). For $\theta_i = 41°$, too small or too large $\theta_g$ may not achieve switching performance. Transmission increases with $\theta_g$, corresponding to *on* configuration of MAS. It approaches the maximal value at $\theta_g = 45°$, but decreases when $\theta_g$ is further increased. Transmission at $\theta_g = 45°$ is higher than $\theta_g = 90°$, which agrees with Fig. 2(a). There is a massive gain in transmission of MAS from $\theta_g = 90°$ to 40° for the *on* configuration. However, for $\theta_i = 21°$, 61°, 81°, respectively, the transmissions can be achieved when $\theta_g$ is increased from 0° to 90°. MAS could not switch *on* and *off* for these incident angles by turning the grating angle. We thus choose the incident angle as $\theta_i = 41°$ and the grating angles as $\theta_g = 90°$ and 0° to achieve *on* and *off* of MAS in the study.

Furthermore, the thickness $L$ of MAS is less than wavelength, differing from previous acoustic switching arrays based on Bragg scattering [21–24]. We compare the *on* and *off* performance of MAS with that of the Bragg scattering structure, as shown in Fig. 2(d). In order to quantify the switching performance, we define the coefficient of switch as

$$S_C = 10\lg\frac{T_{\text{on}}^2}{T_{\text{off}}^2},$$

where $T_{\text{off}}$ and $T_{\text{on}}$ are the transmitted pressure amplitudes at $x = 0.07$ (m) for *off* and *on*, respectively. From the simulation results without noise, $S_c$ shows the dependence on incident angle $\theta_i$ and grating angle $\theta_g$ [Fig. 2(b)]. In comparison with $\theta_i = 21°$, 61°, and 81°, respectively, $\theta_i = 41°$ can produce much higher $S_c$, and thus MAS switch *on* and *off* by turning the grating angle. In addition, there is a massive gain in $S_c$ with the increase of $\theta_g$ for the *on* configuration. In comparison with the low transmission at $\theta_g = 0°$ (*off*), MAS would lead to high switching coefficients within wide grating angle range. There is a massive gain in transmission within wide grating angle range for the *on* configuration, which would have a direct benefit on $S_c$. For $S_c = 10$ (dB), the thickness of the Bragg scattering structure is 75.7 (mm), which is much thicker than $L = 12.5$ (mm) of the metasurface. Thus, MAS offers the advantage to significantly decrease the structure thickness for underwater acoustic manipulation.

To show how other system parameters tune MAS, we switched on and off the MAS in Fig. 3(a) by changing (I) the grating filling rate $A/B$, (II) PMMA plate thickness $d/D$, and (III) coupling distance $d_0/D$. A significantly low $d_0/D$ did not impact switching performance, while decreasing both $A/B$ and $d/D$ significantly changed the acoustic fields at *off* configuration. The phase patterns in Fig. 3(a) are

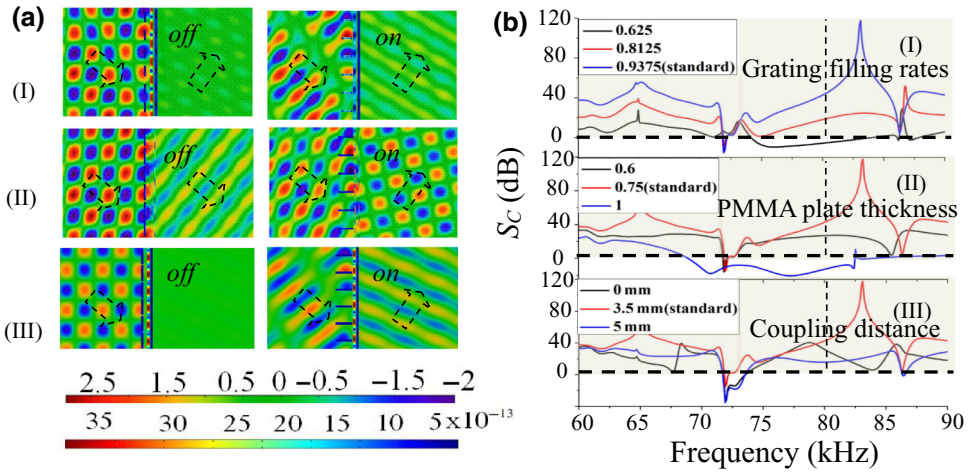


FIG. 3. Tuning MAS. (a) Acoustic switching at frequency 80 kHz for (I) $A/B = 0.625$, (II) $d/D = 0.25$, and (III) $d_0/D = 0.005$. (b) Broadband performances of MAS, where the grating filling rates (0.625, 0.8125, and 0.9375), PMMA plate thicknesses (0.6, 0.75, and 1), and the coupling distances [0 (mm), 3.5 (mm), and 5 (mm)] are used for comparisons.

related to the superposition of incident and reflected waves. In addition, different diffraction modes of the acoustic grating also contribute these phase patterns. For the default MAS parameter values, $S_c$ has maximum value of 100 (dB) and averaged value of 50 (dB) within the broad frequency band [Fig. 3(b)]. Thus, MAS overcomes the narrowband limitation of the Bragg scattering systems.

To verify the switching effect of MAS, we perform underwater acoustic transmission experiments in a 1.5 (m) × 1 (m) × 1 (m) anechoic water tank [Fig. 4(a)]. In order to reduce multiple reflections caused by the walls of the water tank and approach the semifree acoustic field, we install noise-canceling wedge materials at four sides and at the bottom of the tank. These materials functioned well to reduce the reflected signals when frequency is above 50 (kHz). We fabricate the acoustic grating as 500 (mm) × 15 (mm) × 2 (mm) and the PMMA plates as 500 (mm) × 500 (mm) × 3 (mm). MAS is clamped by a scale plate extending out of water. An ultrasound transducer transmitted a tone-burst acoustic signal with the pulse interval of 120 ms and the frequency range from 60 (kHz) to 80 (kHz). The incident angle of the acoustic wave is experimentally measured in 1° steps. After transmitting through MAS, the signal is received by a hydrophone (8103, B&K, Denmark) at the distance of 28 (cm) and displayed on the oscilloscope. Power amplifier (2635, B&K, Denmark) is

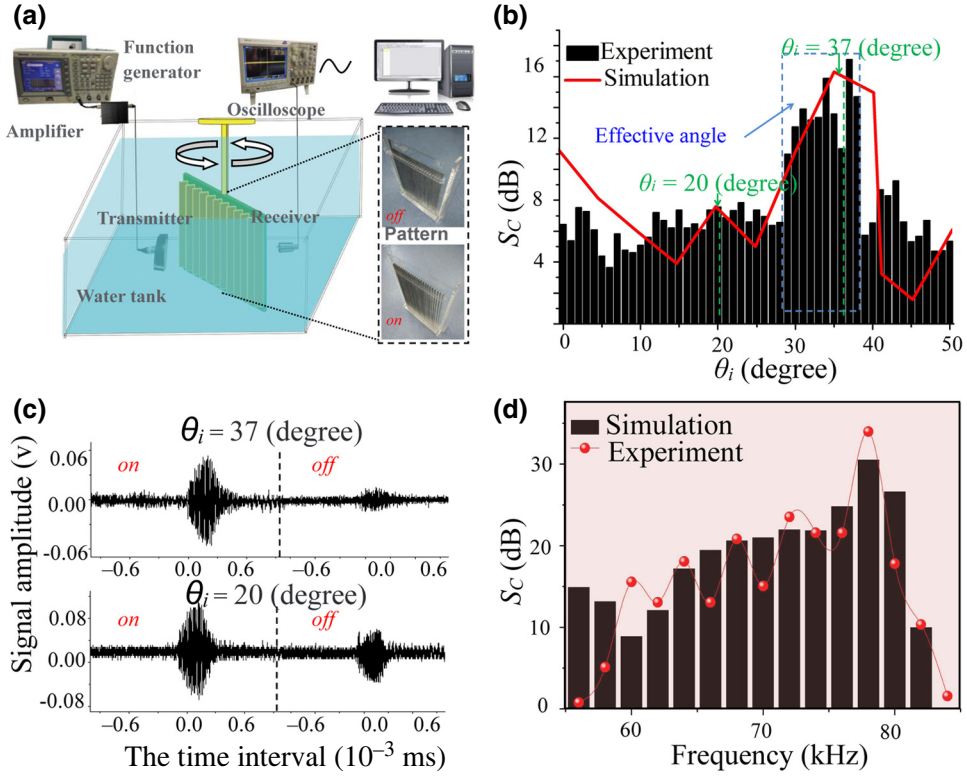


FIG. 4. Acoustic switching experiments. (a) Systematic diagram of the experiment and the *off* and *on* patterns of MAS. (b) Dependence of $S_c$ on incident angle for experimental measurements and numerical simulations for frequency 80 (kHz). (c) Comparison of the transmitted waveforms through MAS for incident angles $\theta_i = 37°$ (upper) and 20° (lower). (d) Broadband switching performances of MAS of experimental measurements and numerical simulations for $\theta_i = 37°$.

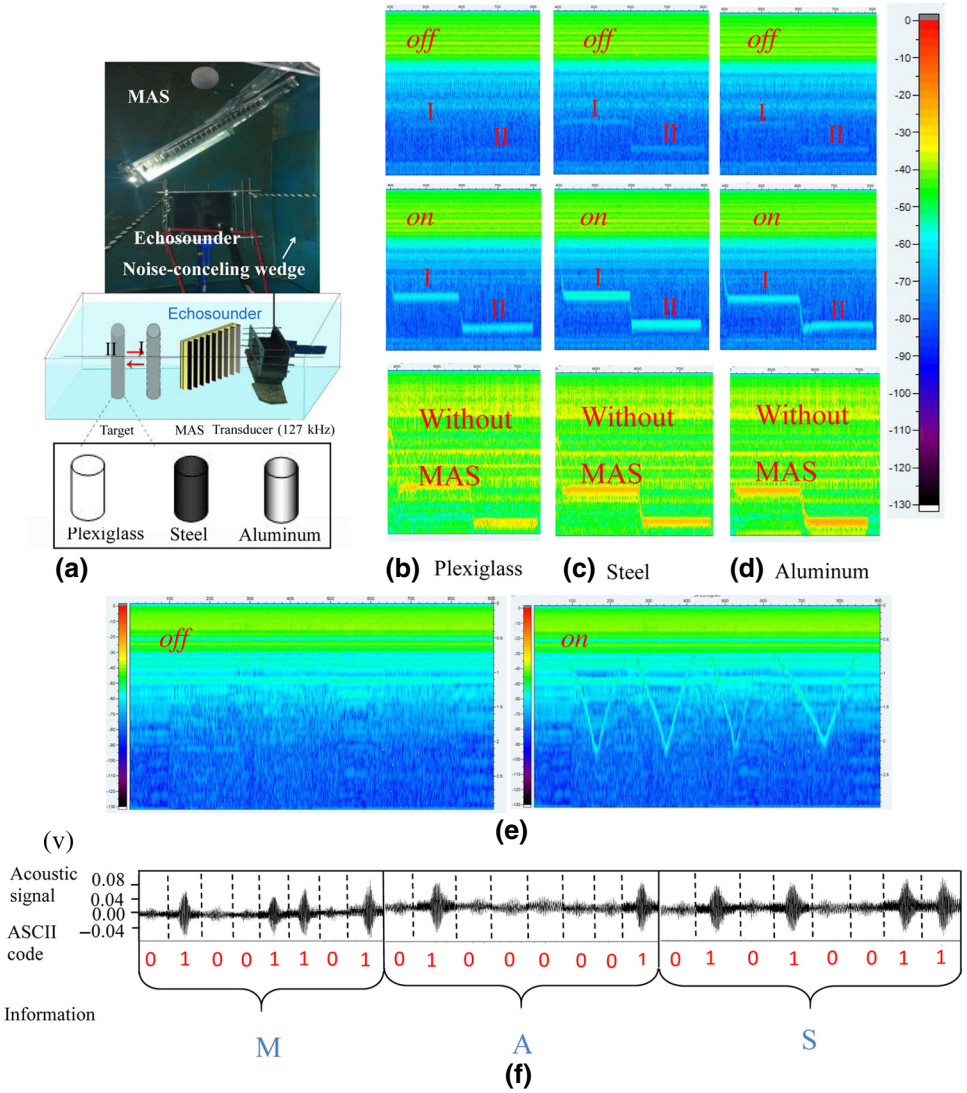


FIG. 5. Underwater applications of MAS. (a) Photographs of the MAS detecting underwater targets. Switching *on* and *off* the MAS to control the target detection for (b) plexiglass, (c) steel, and (d) aluminum targets, where I and II correspond to the target distances of (I) 2 (m) and (II) 2.5 (m) from the source, respectively. (e) Target detection control of MAS at *off* and *on*. (f) Acoustic modulation by MAS into the bit sequence"0100110101000001010 10011", where "0" and "1" represents the signal amplitude is above and below the dashed line.

used to improve the signal-to-noise ratio. The signal is then $A/D$ converted with the sampling rate of 1 (MHz) and processed by a computer. The signals at each trial are measured four times to reduce noises. In experiments, we tune the incident angle but fix the grating filling rate, coupling distance, and PMMA plate thickness to achieve "*on*" and "*off* ", and then the MAS structure might be tunable. We measure the effective angles for low transmissions by continuously increasing incident angle $\theta_i$. Their corresponding computer simulation results are also given for comparison [Fig. 4(b)]. When $\theta_i$ is within the range of 29–38°, $S_c$ is increased over 12 (dB). The measured angle range of the forbidden band qualitatively agreed with the theoretical prediction in Fig. 1(b). Their slight difference may be associated with the measurement errors of plate thickness and incident angle. For $\theta_i = 37°$, switching performance is significantly improved, however, it is not effective for $\theta_i = 20°$ as shown in Fig. 4(c), where the central frequency is 80 (kHz) and $S_c$ is about 6.3 (dB). Furthermore, for $\theta_i = 37°$, $S_c$ changed between 15 (dB) to 30 (dB) when the frequency is increased from 60 (kHz) to 80 (kHz). Its maximal value is 33.5 (dB) for frequency 78 (kHz) [Fig. 4(d)]. In addition, we add white noise to simulations. Figures 3 and 4 give the simulation results without and with noise, respectively. The simulation results under the noisy condition are better compared with the experimental measurements where white noise led to the signal-to-noise ratio of about 15 (dB). As shown in Fig. 8, noise might significantly decrease the coefficient of switching. Qualitative consistency of $S_c$ between experimental measurements and numerical simulations can be found.

We investigate underwater acoustic applications of MAS in Fig. 5(a). Experiments are carried out in a 4 (m) × 5 (m) × 0.8 (m) water pool by using a single beam echosounder (BioSonics, Seattle, WA, USA) with the center frequency of 123 (kHz). Three targets with materials including plexiglass, steel, and aluminum are detected in Figs. 5(b)–5(d), respectively, where vertical axis represents detection distance (m), horizontal axis represents time, and color bar gives backscattered signal amplitude in dB. Each

target with a diameter of 5 (cm) and length of 40 (cm) is placed at distances of (I) 2 (m) and (II) 2.5 (m) from the echosounder. For plexiglass target, MAS successfully switched *on* and *off* echosounder detection. While, for steel and aluminum targets, MAS is less efficient due to their higher scattering capabilities. For all these targets, detected intensities at *on* are more than 15 (dB) higher than those at *off*. The target movement at *on* is clearly captured [Fig. 5(e)]. We also measure the target intensity of the echosounder without MAS. Although the echosounder detected targets, the measured signals are significantly perturbed by the waves whose incident angles are out of the effective angles in Fig. 4(b). Clearly, MAS reduced these perturbations and improved the detection performance, as shown in Fig. 5. Furthermore, MAS modulated acoustic waves into a binary sequence of 1's and 0's [Fig. 5(f)], where "1" corresponds to the signal amplitude above the dashed line, while "0" corresponds to the amplitude below the dashed line. We manually switch the grating angle of MAS. As a demonstration, we apply the modulation speed of 1 bit/s, while higher modulation speed may be achieved by using a high-speed mechanical motor. We experimentally record the acoustic signals during a couple of switches and do not normalize the signals for each switch. By switching acoustic grating according to the bit sequence "010011010100000101010011" (that is, the information "MAS"), acoustic wave is digitized. It shows the reproducibility of the MAS setup. The achieved digital encoding suggests the potential application of MAS in underwater acoustic communication. In addition, MAS might have a different function with acoustic diode. Previous studies have applied acoustic diode to achieve high transmission in one incident direction, but low transmission in the opposite direction [10,17]. However, MAS only controls the one-direction acoustic transmission by turning the grating angle, but does not consider the opposite direction. In particular, for *off* configuration, MAS can not achieve asymmetric transmission since the acoustic grating is almost closed and wave transmission is forbidden. The broadband MAS might be applied as a thin device to control noise radiation.

## III. CONCLUSION

In summary, we demonstrate that MAS effectively switched on and off underwater wave propagation even when the device thickness is less than wavelength. Full-wave simulations show that acoustic diffraction of the grating and mode conversion of the PMMA-water structure led to broadband-switching performance, which might not be found in airborne metamaterials. The device can be tuned when the grating angle, incident angle, grating filling rate, coupling distance, and PMMA plate thickness are changed. Furthermore, MAS experimentally achieved broadband switching to control underwater acoustic waves in order to detect plexiglass, steel, and aluminum targets, and to produce binary digital encoding. This design might provide another class of metasurface with vast underwater applications including noise control, acoustic communication, target detection, etc.

## ACKNOWLEDGMENTS

This work is financially supported in part by National Key Research and Development Program of China 2018YFC1407505 and 2018YFC1407504, the National Natural Science Foundation of China (Grants No. 41676023, No. 41276040, and No. 11604128). P.Z.C. would like to thank Zhongchang Song, Erqian Dong, Xiaohui Xu and Xiaofan Du for their helpful assistance in experiments.

## APPENDIX

### A. Transfer matrix method to derive the low-frequency transmission property of the PMMA-water system

To solve wave propagation in the PMMA-water system, we apply the transfer matrix method for plane waves [17]. Figure 6(a) depicts the system, where $x$ and $y$ axes are normal and parallel to the interfaces, respectively, and a plane longitudinal wave propagates from the left side through the $N$ PMMA-water layers and travels to the right side. The displacement field $\mathbf{v}$ can be separated into scalar and vector potentials: $\mathbf{v} = \text{grad}\ \Phi + \text{rot}\ \Psi$ and $\text{div}\Psi = 0$. For the $j$th layer, the longitude wave with $\Phi_1$ passes through the liquid-solid interface at $x_j$ and is converted to the longitude wave $\Phi_2$ and shear wave $\Psi_2$ in PMMA. Then, the waves are converted back to the longitudinal pressure wave $\Phi_3$ through the liquid-solid interface at $x_j + d_{\mathrm{I}}$ in the water and then propagates into $\Phi_4$ at $x_{j+1} = x_j + d_{\mathrm{I}} + d_{\mathrm{II}}$. By omitting the time factor $e^{j\omega t}$, these scalar and vector potentials can be obtained as

$$\Phi_1 = \Phi_{1i} e^{-j\,(k_{\mathrm{I}L}\cos\theta_{\mathrm{I}L}x + k_{\mathrm{I}L}\sin\theta_{\mathrm{I}L}z)} + \Phi_{1r} e^{-j\,(-k_{\mathrm{I}L}\cos\theta_{\mathrm{I}L}x + k_{\mathrm{I}L}\sin\theta_{\mathrm{I}L}z)}, \tag{A1a}$$

$$\Phi_2 = \Phi_{2i} e^{-j\,(k_{\mathrm{II}L}\cos\theta_{\mathrm{II}L}x + k_{\mathrm{II}L}\sin\theta_{\mathrm{II}L}z)} + \Phi_{2r} e^{-j\,(-k_{\mathrm{II}L}\cos\theta_{\mathrm{II}L}x + k_{\mathrm{II}L}\sin\theta_{\mathrm{II}L}z)}, \tag{A1b}$$

$$\Psi_2 = \Psi_{2i} e^{-j\,(k_{\mathrm{II}T}\cos\theta_{\mathrm{II}T}x + k_{\mathrm{II}T}\sin\theta_{\mathrm{II}T}z)} + \Psi_{2r} e^{-j\,(-k_{\mathrm{II}T}\cos\theta_{\mathrm{II}T}x + k_{\mathrm{II}T}\sin\theta_{\mathrm{II}LT}z)}, \tag{A1c}$$

$$\Phi_3 = \Phi_{3i} e^{-j\,(k_{\mathrm{I}L}\cos\theta_{\mathrm{I}L}x + k_{\mathrm{I}L}\sin\theta_{\mathrm{I}L}z)} + \Phi_{3r} e^{-j\,(-k_{\mathrm{I}L}\cos\theta_{\mathrm{I}L}x + k_{\mathrm{I}L}\sin\theta_{\mathrm{I}L}z)}, \tag{A1d}$$

$$\Phi_{4i} = \Phi_{3i} e^{-j\,k_{\mathrm{I}L}\cos\theta_{\mathrm{I}L}d_{\mathrm{I}}} + \Phi_{3r} e^{j\,k_{\mathrm{I}L}\cos\theta_{\mathrm{I}L}d_{\mathrm{I}}}, \tag{A1e}$$

where $k_{\mathrm{I}L}$, $k_{\mathrm{II}L}$, $k_{\mathrm{II}T}$ denotes the longitude wave number in the water, the longitude wave number in the PMMA,

and the transverse wave number in PMMA, and $\theta_{1L}$, $\theta_{\mathrm{II}L}$, $\theta_{\mathrm{II}T}$ denotes the corresponding oblique incident angle. $\Phi_{1i}$, $\Phi_{2i}$, $\Phi_{3i}$, and $\Psi_{2i}$ represent the incident wave amplitudes, while $\Phi_{1r}$, $\Phi_{2r}$, $\Phi_{3r}$, and $\Psi_{2r}$ represent the reflected wave amplitudes.

The boundary conditions of the continuous normal velocity and the balance of the stresses at the interface $x_i$ and $x = x_i + d_{\mathrm{I}}$ satisfy

$$\left.\frac{\partial \Phi_1}{\partial x}\right|_{x=x_i} = \left.\frac{\partial \Phi_2}{\partial x} - \frac{\partial \Psi_2}{\partial z}\right|_{x=x_i},$$
$$T_{1xx}|_{x=x_i} = T_{2xx}|_{x=x_i}, \quad T_{1xz}|_{x=x_i} = T_{2xz}|_{x=x_i}, \tag{A2a}$$
$$\left.\frac{\partial \Phi_3}{\partial x}\right|_{x=x_i+d_{\mathrm{I}}} = \left.\frac{\partial \Phi_2}{\partial x} - \frac{\partial \Psi_2}{\partial z}\right|_{x=x_i+d_{\mathrm{I}}},$$
$$T_{3xx}|_{x=x_i+d_{\mathrm{I}}} = T_{4xx}|_{x=x_i+d_{\mathrm{I}}},$$
$$T_{3xz}|_{x=x_i+d_{\mathrm{I}}} = T_{4xz}|_{x=x_i+d_{\mathrm{I}}}, \tag{A2b}$$

where

$$T_{1xx} = j\rho_{\mathrm{I}}\omega\Phi_1,$$
$$T_{2xx} = \frac{\rho_{\mathrm{II}}}{j\omega}\left[-\omega^2\Phi_2 - 2c_{\mathrm{II}T}^2\left(\frac{\partial^2\Psi_2}{\partial x\partial z} + \frac{\partial^2\Phi_2}{\partial z^2}\right)\right], \quad T_{1xz} = 0,$$

and

$$T_{2xz} = \frac{c_{\mathrm{II}T}^2}{j\omega}\left(\frac{\partial^2\Psi_2}{\partial x^2} - \frac{\partial^2\Psi_2}{\partial z^2} + 2\frac{\partial^2\Phi_2}{\partial x\partial z}\right),$$
$$T_{3xx} = j\rho_{\mathrm{I}}\omega\Phi_3,$$
$$T_{4xx} = \frac{\rho_{\mathrm{II}}}{j\omega}\left[-\omega^2\Phi_2 - 2c_{\mathrm{II}T}^2\left(\frac{\partial^2\Psi_2}{\partial x\partial z} + \frac{\partial^2\Phi_2}{\partial z^2}\right)\right],$$
$$T_{3xz} = 0, \quad \text{and}$$
$$T_{2xz} = \frac{c_{\mathrm{II}T}^2}{j\omega}\left(\frac{\partial^2\Psi_2}{\partial x^2} - \frac{\partial^2\Psi_2}{\partial z^2} + 2\frac{\partial^2\Phi_2}{\partial x\partial z}\right).$$

$c_{\mathrm{II}T}$ is the sound velocity of transverse wave in PMMA. $\rho_{\mathrm{I}}$ and $\rho_{\mathrm{II}}$ are the density of water and PMMA, respectively.

From the boundary condition of normal speed continuity, the Snell law can be obtained as

$$k_{1L}\sin(\theta_{1L}) = k_{\mathrm{II}L}\sin(\theta_{\mathrm{II}L}) = k_{\mathrm{II}T}\sin(\theta_{\mathrm{II}T}). \tag{A3}$$

In addition, the boundary conditions of stress balance leads to the transfer matrix $T_j$ from $\Phi_1$ to $\Phi_4$ as

$$\Phi_1 = T_j\Phi_4, \tag{A4}$$

where

$$T_j = M_1^{-1}M_2M_4^{-1}M_3U^{-1},$$
$$M_1 = \begin{pmatrix} k_{1L}\cos\theta_{1L} & -k_{\mathrm{II}L}\cos\theta_{\mathrm{II}L} \\ 1 & 1 \end{pmatrix},$$
$$M_2 = \begin{pmatrix} k_{\mathrm{II}L}\cos\theta_{\mathrm{II}L} & -k_{\mathrm{II}L}\cos\theta_{\mathrm{II}L} & -k_{\mathrm{II}T}\sin\theta_{\mathrm{II}T} & -k_{\mathrm{II}T}\sin\theta_{\mathrm{II}T} \\ \frac{\rho_{\mathrm{II}}}{\rho_{\mathrm{I}}}\cos 2\theta_{\mathrm{II}T} & \frac{\rho_{\mathrm{II}}}{\rho_{\mathrm{I}}}\cos 2\theta_{\mathrm{II}L} & -\frac{\rho_{\mathrm{II}}}{\rho_{\mathrm{I}}}\sin 2\theta_{\mathrm{II}T} & \frac{\rho_{\mathrm{II}}}{\rho_{\mathrm{I}}}\sin 2\theta_{\mathrm{II}T} \end{pmatrix},$$
$$M_3 = \begin{pmatrix} k_{1L}\cos\theta_{1L} & -k_{1L}\cos\theta_{1L} \\ 1 & 1 \\ 0 & 0 \\ 0 & 0 \end{pmatrix},$$
$$M_4 = \begin{pmatrix} k_{\mathrm{II}L}\cos\theta_{\mathrm{II}L}e^{-jk_{\mathrm{II}L}\cos\theta_{\mathrm{II}L}d_{\mathrm{II}}} & -k_{\mathrm{II}L}\cos\theta_{\mathrm{II}L}e^{jk_{\mathrm{II}L}\cos\theta_{\mathrm{II}L}d_{\mathrm{II}}} & -k_{\mathrm{II}L}\cos\theta_{\mathrm{II}L}e^{-jk_{\mathrm{II}L}\cos\theta_{\mathrm{II}L}d_{\mathrm{II}}} & -k_{\mathrm{II}L}\cos\theta_{\mathrm{II}T}e^{jk_{\mathrm{II}T}\cos\theta_{\mathrm{II}T}d_{\mathrm{II}}} \\ \frac{\rho_{II}}{\rho_I}\cos 2\theta_{\mathrm{II}T}e^{-jk_{\mathrm{II}L}\cos\theta_{\mathrm{II}L}d_{\mathrm{II}}} & \frac{\rho_{II}}{\rho_I}\cos 2\theta_{\mathrm{II}T}e^{jk_{\mathrm{II}l}\cos\theta_{\mathrm{II}l}d_{\mathrm{II}}} & -\frac{\rho_{II}}{\rho_I}\sin 2\theta_{\mathrm{II}T}e^{-jk_{\mathrm{II}T}\cos\theta_{\mathrm{II}T}d_{\mathrm{II}}} & \frac{\rho_{II}}{\rho_I}\sin 2\theta_{\mathrm{II}T}e^{jk_{\mathrm{II}T}\cos\theta_{\mathrm{II}T}d_{\mathrm{II}}} \\ k_{\mathrm{II}L}^2\sin 2\theta_{\mathrm{II}L} & -k_{\mathrm{II}L}^2\sin 2\theta_{\mathrm{II}L} & k_{\mathrm{II}T}^2\cos 2\theta_{\mathrm{II}T} & k_{\mathrm{II}T}^2\cos 2\theta_{\mathrm{II}T} \\ k_{\mathrm{II}L}^2\sin 2\theta_{\mathrm{II}L}e^{-jk_{\mathrm{II}L}\cos\theta_{\mathrm{II}L}d_{\mathrm{II}}} & -k_{\mathrm{II}L}^2\sin 2\theta_{\mathrm{II}L}e^{jk_{\mathrm{II}L}\cos\theta_{\mathrm{II}L}d_{\mathrm{II}}} & k_{\mathrm{II}T}^2\cos 2\theta_{\mathrm{II}T}e^{-jk_{\mathrm{II}T}\cos\theta_{\mathrm{II}T}d_{\mathrm{II}}} & k_{\mathrm{II}T}^2\cos 2\theta_{\mathrm{II}T}e^{jk_{\mathrm{II}t}\cos\theta_{\mathrm{II}T}d_{\mathrm{II}}} \end{pmatrix},$$
$$U = \begin{pmatrix} e^{-jk_{1L}\cos\theta_{1L}d_{\mathrm{I}}} & 0 \\ 0 & e^{jk_{1L}\cos\theta_{1L}d_{\mathrm{I}}} \end{pmatrix}.$$

Therefore, two state vectors of the first and $N$th layers of PMMA are connected as

$$\Phi_0 = T_{1,N}\Phi_N, \tag{A5}$$

where $T_{1,N} = T_1 T_2 \cdots T_N$. The transfer matrix $T_{1,N}$ connects the first and last units of the PMMA system, leading to the total transmission and reflection rates as

$$T_{1,N} = \begin{pmatrix} \frac{1}{t} & \frac{r^*}{t^*} \\ \frac{r}{t} & \frac{1}{t^*} \end{pmatrix}, \tag{A6}$$

where $t$ and $r$ are transmission and reflection coefficients, $T_N = |t|^2$ and $R_N = |r|^2$ define the transmission and reflection rates, satisfying $T_N + R_N = 1$. For two PMMA-water layers ($N = 2$), $L \ll \lambda$ leads to the metasurface in Fig. 1(a). Using the above transfer matrix method, we can derive transmissions of the PMMA-water system ($N = 8$) at different oblique incident angles in Fig. 2. As a comparison, the transmission result of the PMMA-air metamaterial is given [Fig. 6(b)]. Clearly, low-frequency forbidden transmission in the PMMA-water metasurface can not be found in the airborne metamaterial. A previous study [16] has investigated acoustic switching performance in airborne metamaterials. The device is applied in air, differing from the underwater metasurface in this study. Direct comparison between these two designs might be difficult since they may have different physical mechanisms and applications. For example, low-frequency forbidden transmission in the underwater MAS can not be observed in PMMA-air structure [Figs. 1 and 6(b)]. Furthermore, using the transfer matrix method, acoustic mode conversion of the PMMA-water system can be analyzed. The transmission

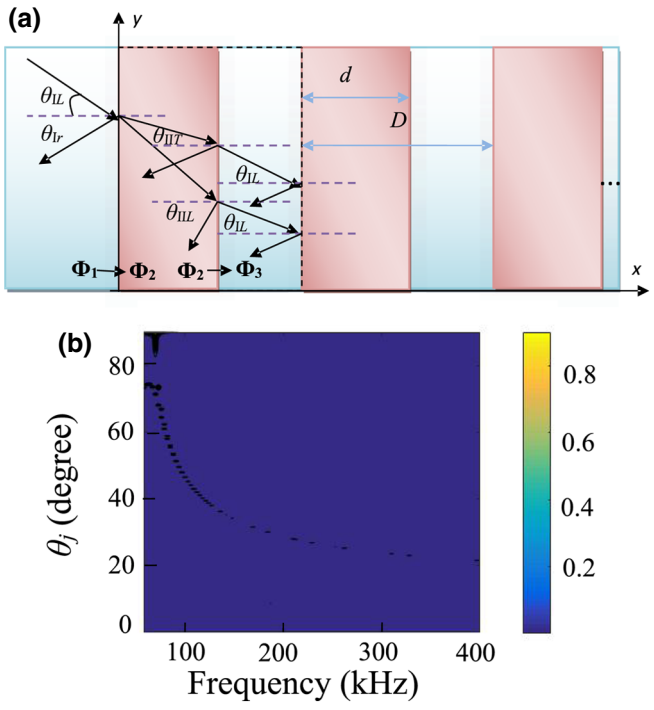


FIG. 6. (a) Systematic diagram of PMMA-water system. (b) Transmission coefficient as a function of frequency and incident angle of the PMMA-air metamaterial ($N = 2$).

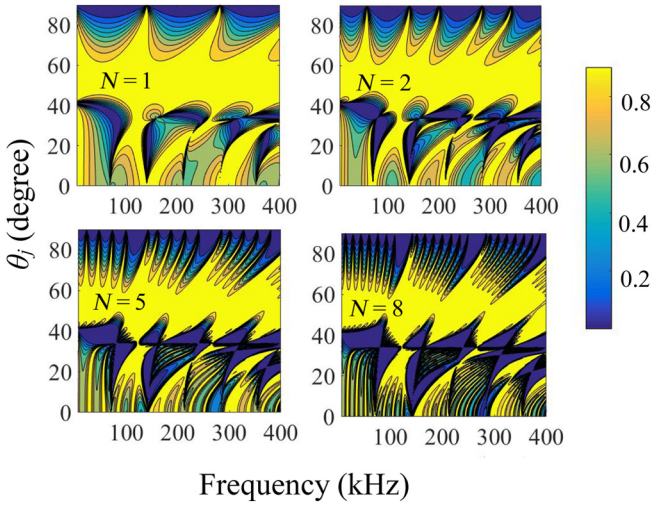


FIG. 7. Transmission coefficients of the PMMA-water systems with $N = 1$, 2, 5, and 10, respectively.

coefficients are compared with $N = 1$, 2, 5, and 10, respectively, as shown in Fig. 7. Lamb waves with various modes, such as symmetric and asymmetric types can be clearly found.

### B. The influence of noise on simulation results

In experiments, noise inevitably exists. To simulate the influence of noise, we add white noise to the full-wave simulations by using COMSOL Multiphysics. Figures 3 and 4(d) present the simulation results under different noise conditions. Figure 3 gives the simulation results without noise. However, Fig. 4(d) gives the simulation result under the noisy condition. It better compared with the experimental measurements where white noise led to the signal-to-noise ratio about 15 (dB). As shown in Fig. 8, noise significantly

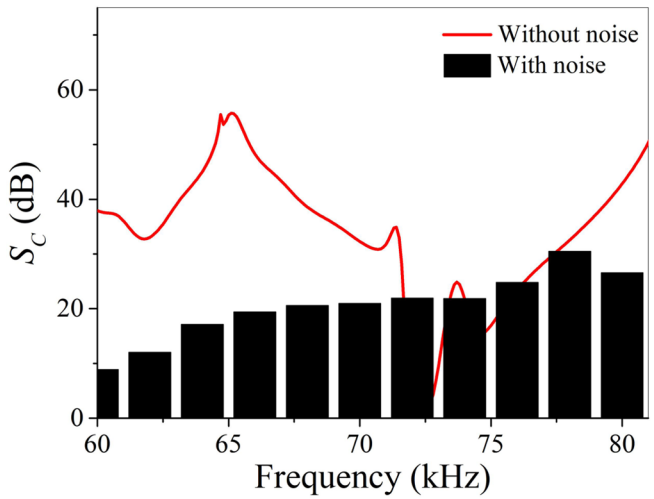


FIG. 8. Simulation results of MAS with and without noise.

decreases the coefficient of switching within the frequency range applied in the experiments. In Fig. 4(d), the simulation with noise better corresponded to the experimental measurement.


[1] J. B. Pendry, Negative Refraction Makes a Perfect Lens, Phys. Rev. Lett. **85**, 3966 (2000).

[2] H. Ge, M. Yang, C. Ma, M. H. Lu, Y. F. Chen, Nicholas Fang, and Ping Sheng, Breaking the barriers: Advances in acoustic functional materials, national, Natl. Sci. Rev. **5**, 159 (2017).

[3] Y. F. Chen, Negative bi-refraction of acoustic waves in sonic crystals, Nat. Mater. **6**, 744 (2008).

[4] N. Kaina, F. Lemoult, M. Fink, and G. Lerosey, Negative refractive index and acoustic superlens from multiple scattering in single negative metamaterials, Nature. **525**, 77 (2015).

[5] J. J. Park, C. M. Park, K. J. B. Lee, and S. H. Lee, Acoustic superlens using membrane-based metamaterials, Appl. Phys. Lett. **106**, 3966 (2015).

[6] S. Zhang, L. Yin, and N. X. Fang, Focusing Ultrasound with an Acoustic Metamaterial Network, Phys. Rev. Lett. **102**, 194301 (2009).

[7] E. Dong, Y. Zhang, Z. Song, T. Zhang, C. Chen, and N. X. Fang, Physical modeling and validation of porpoises' directional emission via hybrid metamaterials, Natl. Sci. Rev. **6**, 921 (2019).

[8] S. Zhang, C. G. Xia, and N. X. Fang, Broadband Acoustic Cloak for Ultrasound Waves, Phys. Rev. Lett. **106**, 024301 (2011).

[9] Y. Bi, H. Jia, Z. Sun, Y. Yang, H. Zhao, and J. Yang, Experimental demonstration of three-dimensional broadband underwater acoustic carpet cloak, Appl. Phys. Lett. **112**, 223502 (2018).

[10] B. Liang, B. Yuan, and J. C. Cheng, Acoustic Diode: Rectification of Acoustic Energy Flux in One-Dimensional Systems, Phys. Rev. Lett. **103**, 104301 (2009).

[11] C. Shi, M. Dubois, Y. Wang, and X. Zhang, High-speed acoustic communication by multiplexing orbital angular momentum, Proc. Natl. Acad. Sci. U. S. A. **114**, 7250 (2017).

[12] J. Mei, X. Zhang, and Y. Wu, Ultrathin metasurface with high absorptance for waterborne sound, J. Appl. Phys. **123**, 091710 (2018).

[13] Y. Li, B. Liang, Z. Gu, X. Zou, and J. Cheng, Reflected wavefront manipulation based on ultrathin planar acoustic metasurfaces, Sci. Rep. **3**, 2546 (2013).

[14] J. Zhao, B. Li, Z. N. Chen, and W. Cheng, Redirection of sound waves using acoustic metasurface, Appl. Phys. Lett. **103**, 151604 (2013).

[15] N. Yu, P. Genevet, M. A. Kate, F. Aieta, J. P. Tetienne, F. Capasso, and Z. Gaburro, Light propagation with phase discontinuities: Generalized laws of reflection and refraction, Science **334**, 333 (2011).

[16] S. Babaee, N. Viard, P. Wang, P. Wang, N. X. Fang, and K. Bertoldi, Harnessing deformation to switch on and off the propagation of sound, Adv. Mater. **28**, 1630 (2016).

[17] S. Zhang, Y. Zhang, Y. Guo, Y. Leng, W. Feng, and W. Cao, Realization of Subwavelength Asymmetric Acoustic Transmission Based on low-Frequency Forbidden Transmission, Phys. Rev. Appl. **5**, 034006 (2016).

[18] S. Zhang, B. Xu, G. Hu, S. Cui, H. He, and W. Cao, A subwavelength asymmetric acoustic design for waveform-preserved highly forward transmission, AIP. Adv. **8**, 085102 (2018).

[19] J. Gao, J. C. Cheng, and B. Li, Propagation of Lamb waves in one-dimensional quasiperiodic composite thin plates: A split of phonon band gap, Appl. Phys. Lett. **90**, 111908 (2007).

[20] V. Twersky, On scattering of waves by the infinite grating of circular cylinders, IEEE Trans. Antenn. Propag. **10**, 737 (1962).

[21] Y. Li, H. Shen, L. Zhang, Y. Su, and D. Yu, Control of low-frequency noise for piping systems via the design of coupled band gap of acoustic metamaterials, Phys. Lett. A. **380**, 2322 (2016).

[22] C. J. Naify, C. M. Chang, G. Mcknight, and S. Nutt, Transmission loss and dynamic response of membrane-type locally resonant acoustic metamaterials, J. Appl. Phys. **108**, 114905 (2010).

[23] A. O. Krushynska, V. G. Kouznetsova, and M. G. D. Geers, Towards optimal design of locally resonant acoustic metamaterials, J. Mech. Phys. Solids. **71**, 179 (2014).

[24] E. Dong, Y. Zhou, Y. Zhang, and H. Chen, Bioinspired Conformal Transformation Acoustics, Phys. Rev. Appl. **13**, 024002 (2020).